RSC Advances

PAPER

View Article Online
View Journal | View Issue

Cite this: *RSC Adv.*, 2026, **16**, 18083

Development of sphere-shaped bimetallic $Ti_{0.5}Sr_{0.5}O_3$ as an efficient bifunctional electrocatalyst for overall water splitting performance in alkaline media

Kayalvizhi Rajagopal and Abirami Natarajan *

Received 9th January 2026
Accepted 28th March 2026

DOI: 10.1039/d6ra00224b

rsc.li/rsc-advances

Developing low-cost, highly active electrocatalysts for electrochemical water splitting is crucial for decreasing the demand for energy in the future. Water splitting has been addressed as a feasible option for storing electrical energy. Researchers are interested in designing non-toxic, high-performance, and cost-effective catalysts for the oxygen evolution reaction (OER) and the hydrogen evolution reaction (HER). Herein, spherical structured $Ti_{0.5}Sr_{0.5}O_3$ catalysts, which are materials made from titanium and strontium oxides, are produced using a simple solid-state technique. XRD, Raman, FE-SEM, TEM, XPS, and FT-IR spectroscopy were performed to confirm the crystal structure, morphology, and element composition of the $Ti_{0.5}Sr_{0.5}O_3$. In alkaline electrolyte 1.0 M KOH solution, $Ti_{0.5}Sr_{0.5}O_3$/NF has good OER activity, with an overpotential and a Tafel slope of 299 mV and 152.5 mV dec^{-1}, respectively. It also exhibits strong HER activity, with overpotential and a Tafel slope of 101.6 mV and 179 mV dec^{-1}, respectively. The present research employs an innovative development approach for a low-cost, highly efficient water-splitting catalyst that aligns with the United Nations' Sustainable Development Goal 7 for affordable and clean energy.

1. Introduction

The shortage of energy and destruction of the environment are two of the most significant world problems, intensified by the heavy extraction and use of fossil fuels. The growing requirement for energy, constrained fossil fuel resources, and their associated ecological and socioeconomic effects caused an urgent quest for alternative energy sources.[1] In response, scientists have concentrated on establishing energy conversion and storage systems such as water-splitting cells, supercapacitors, lithium-ion batteries, and metal–air batteries. Among them, electrochemical water splitting is regarded as a sustainable and clean method of manufacturing hydrogen, a green and affordable fuel. Water electrolysis consists of two half-cell reactions: the oxygen evolution reaction (OER) and the hydrogen evolution reaction (HER). The OER's slow kinetics severely constrain overall efficiency, as the oxygen evolution process requires a high overpotential to establish the O–O covalent bond *via* a four-electron transfer mechanism.[2] Noble-metal catalysts, such as iridium- and ruthenium-containing compounds, can efficiently accelerate this reaction, but their high cost and unavailability prevent their widespread application. Transition-metal-based catalysts provide a nonprecious alternative, but their inherent activity toward water oxidation is usually limited. By adapting the electronic structure, the catalytic activity of these materials can be enhanced, leading the path for highly effective and environmentally friendly hydrogen production.

It is imperative to develop sustainable energy sources as alternatives to address the energy crisis and its associated environmental problems. Researchers have extensively studied a number of renewable energy sources, including wind, solar, biopower, and hydropower, as potential sustainable alternatives to fossil fuels. As a result, there is an urgent need to create new methods for converting, storing, and utilizing the electrical energy created.[3] Hydrogen, an energy carrier, can efficiently transform electrical energy into chemical energy (hydrogen fuel) using water electrolysis.[4] This is an intriguing method for meeting the goal of energy conversion and storage. Furthermore, hydrogen has a high gravimetric energy density and produces ecologically favourable combustion products, making it a viable alternative to conventional fossil fuels.[5] On the other hand, hydrogen is produced through natural gas reforming and coal and oil gasification, all of which require the usage of fossil fuels and emit CO_2.[6] To this aim, water splitting appears as an interesting technique for hydrogen production because it is both ecologically friendly and sustainable, in addition to creating high-quality hydrogen (more than 99.9%).[7] Several

Department of Chemistry, College of Engineering and Technology, SRM Institute of Science and Technology, Kattankulathur, Tamil Nadu-603203, India. E-mail: abiramin@srmist.edu.in; Tel: +91 9941223928

factors influence the total efficiency of hydrogen fuel generation, and these are the primary driving forces behind full water electrolysis. Increasing the overall reaction rate creates an external bias of ≤1.23 V against RHE, which exceeds the theoretical value.[8] The OER's four-proton-linked electron ($4e^-$) transport mechanism may explain the observed behavior.[9] Additionally, a three-electrode electrolyzer that is incorporated within a bigger device demonstrates a high conversion efficiency while operating at 1.8–2.0 V. This additional voltage input creates a significant difference between the electrocatalyst's cost and its electrochemical performance. As a consequence, to speed up both half-reactions, it is necessary to have a wide surface area, high stability, a large number of active sites, and consistent adsorption of effective electrocatalysts.[10] While noble-metal catalysts such as Pt, IrO_2, and RuO_2 exhibit excellent performance, their high cost and limited availability hinder large-scale application.[11]

Transition-metal oxides, particularly perovskite-type oxides, have attracted attention as cost-effective alternatives due to their structural versatility, tunable electronic properties, and stability under electrochemical conditions.[12] Transition metal oxides have been shown in both theoretical and practical studies to offer significant potential for water electrolysis.[13] In this context, spherical $Ti_{0.5}Sr_{0.5}O_3$ offers potential as a bifunctional catalyst, combining favorable electronic structure and surface properties for both OER and HER, while utilizing abundant and inexpensive elements. Despite some studies on $Ti_{0.5}Sr_{0.5}O_3$ synthesis and characterization, its bifunctional catalytic performance, mechanistic understanding, and structure–activity relationships remain largely unexplored. Titanium and strontium have received a lot of attention in the field of electrocatalysis compared to other metals, due to their low electronegativity, small particle size, form, strong electrical capacity, increased number of active sites, and wide surface area.[14] Furthermore, the increasing interaction between strontium and titanium enhances superconductivity and chemical stability, suggesting an effective OER/HER reaction pathway. To manufacture the composite catalyst, we took a conventional, solid-state technique. Therefore, this work investigates $Ti_{0.5}Sr_{0.5}O_3$ as a bifunctional electrocatalyst for water splitting, focusing on its synthesis, structural and electronic properties, and electrochemical performance, which reveal its potential as an efficient and sustainable material for hydrogen production. In accordance with the findings of X-ray diffraction, the heterojunction approach is responsible for modifying not only the electrical structure but also the phase formation of bifunctional catalysts. HR-TEM analysis was also utilized in order to evaluate the spherical form of the synthetic composite as well as the quality of its material. In a 1.0 M KOH solution, $Ti_{0.5}Sr_{0.5}O_3$/NF has good OER activity, with an overpotential of 299 mV and a Tafel slope of 152.5 mV dec^{-1}. It also exhibits strong HER activity, with an overpotential of 101.6 mV and a Tafel slope of 179 mV dec^{-1}. Both the ECSA and EIS evaluations revealed that this diverse structure had efficient transportation pathways. These channels are created by increasing the contact area of the two materials and lowering the energy barriers. The LSV approach was also used to analyze the electrochemical behavior of $Ti_{0.5}Sr_{0.5}O_3$/NF on a three-electrode setup. Furthermore, the $Ti_{0.5}Sr_{0.5}O_3$/NF remained durable up to 40 hours. The utilization of transition metals provides a novel approach to the study and design of diverse bifunctional electrocatalysts. This approach has the potential to significantly enhance the bifunctional electrochemical water splitting on a wide scale.

2. Experimental section

2.1 Preparation of $Ti_{0.5}Sr_{0.5}O_3$

The chemicals titanium(IV) butoxide, strontium carbonate, and ethanol were acquired from Aldrich Chemicals. Deionized water purified with the Millipore Milli-Q system was used in all of the investigations in this research. The fact that all of the reagents were of analytical quality meant that there was no need for any additional purification efforts. A typical procedure for preparing spherical-shaped $Ti_{0.5}Sr_{0.5}O_3$/NF was as follows: after 4.7 g strontium carbonate ($SrCO_3$) was accurately weighed, ground, and 10 mL of absolute ethanol was added to the $SrCO_3$ powder, which was well mixed. 5.0 mL of titanium(IV) butoxide was added to the mixture (the molar ratio of Sr to Ti was 1.2 in the reactants), subsequently, vigorously ground for 1 hour for evaporation of ethanol at room temperature, and then the mixture turned into a white slurry. After that, the samples were added to 20 mL of 3 M acetic acid, soaked for 1 h to remove impurities in the products, centrifuged, and washed ultrasonically with distilled water three times, then two times with absolute ethanol and distilled water alternately, and finally dried at 400 °C for 8 h. At 400 °C, composites undergo complete removal of organics without excessive grain growth, full decomposition of nitrates, removal of carbon residues, and formation of the initial oxide network. XRD patterns from Fig. 1a will be provided to show the phase formation process. At 400 °C, the target perovskite phase formed with good crystallinity and no detectable impurity peaks. Higher temperatures significantly improve crystallinity without particle agglomeration. SEM images, Fig. 2a–d corresponding to calcination temperature, will be added to demonstrate the influence of calcination temperature on particle size without agglomeration behaviour. The results indicate that 400 °C provides a good balance between phase formation and microstructural control. In the SI from Fig. S1, the synthesis of $Ti_{0.5}Sr_{0.5}O_3$ was explained.

2.2 Characterization

In order to obtain the XRD measurements, a PAN Analytical X'Pert Pro diffractometer was used. A Quanta 200 FEG FE-SEM was utilized to investigate the surface of the materials that were produced. JEOL model 1010 microscopes were utilized in order to capture images through the transmission electron microscopy methodology. The FT-IR spectra were measured by employing a Fourier transform infrared spectrometer (VERTEX 80v, Bruker). The objective of this investigation was to obtain an improved comprehension of the functional properties of the materials that were synthesized. Interpretation of the Raman spectra was successfully performed with the use of a Raman spectrometer (LabRAM HR Evolution, Horiba) that featured an excitation line with a wavelength of 532 nm.

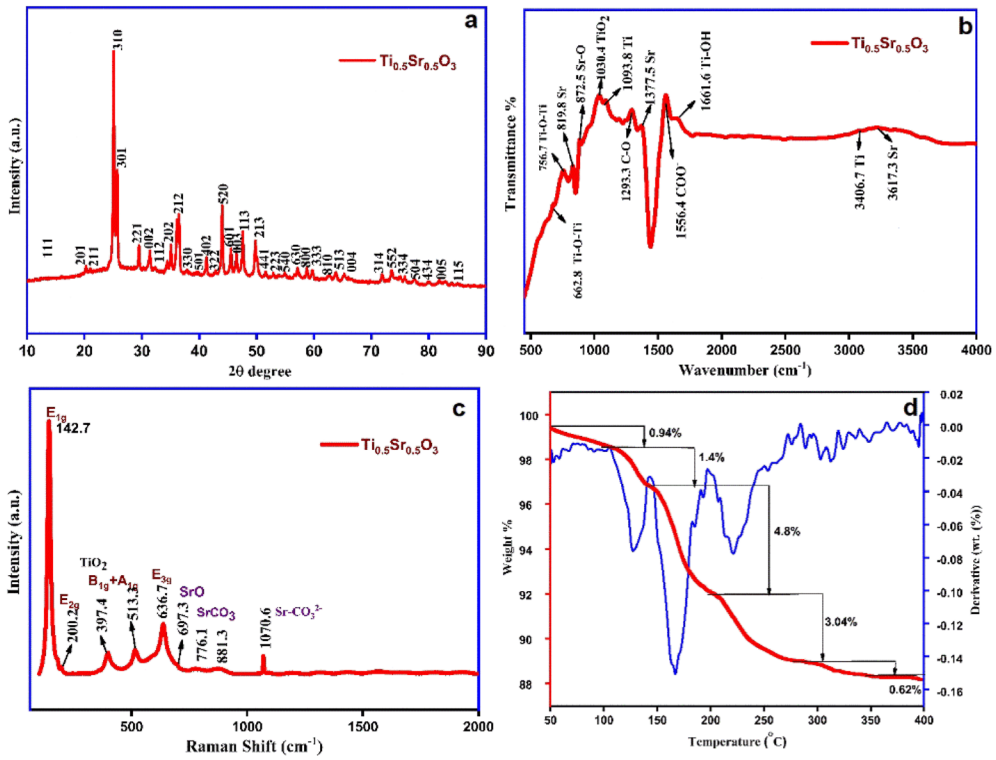

Fig. 1 (a) XRD, (b) FT-IR, (c) Raman spectra, and (d) TGA/DTA analysis of $Ti_{0.5}Sr_{0.5}O_3$.

2.3 Electrocatalytic activity studies

In order to evaluate the electrocatalytic performance of the material that was produced, a three-electrode measurement device was utilized. There is an increasing interaction between strontium and titanium that enhances superconductivity in the system: a working electrode (which is denoted as $Ti_{0.5}Sr_{0.5}O_3$/NF, where $Ti_{0.5}Sr_{0.5}O_3$ represents the spherical catalyst loaded

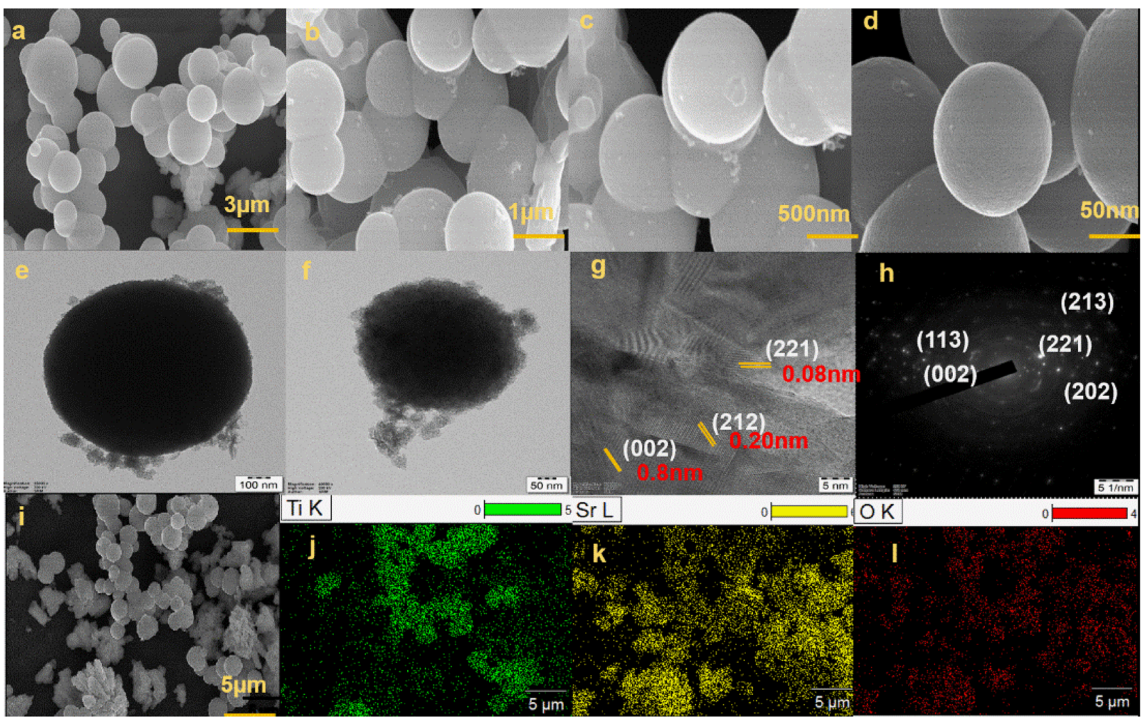

Fig. 2 (a–d) FESEM images; (e and f) TEM images; (g) lattice spacing; (h) selected area electron diffraction pattern; (i–l) elemental mapping of $Ti_{0.5}Sr_{0.5}O_3$.

onto nickel foam (NF) to serve as the conductive substrate during electrochemical characterization), a reference electrode (Ag/AgCl in KCl), and a counter electrode (graphite rod). A Ni foam substrate was used for the application of the material that was manufactured. First, the Ni foam was treated with HCl at a concentration of one milliliter, and then it was washed with distilled water. After that, it was sonicated with ethanol for fifteen minutes, and then it was dried in an oven for six hours. In order to evaluate the electrochemical performance, active materials representing 80% of the total, carbon black representing 10%, and PVDF representing 10% were combined as a binder. After being properly mixed in NMP, the slurry was coated over a Ni foam that was 1 cm^2 in size and 1 cm^2 in thickness. After that, it was dried in an oven at 60 °C for 12 hours. In order to conduct water splitting research, the bulk of the dried foam was measured and collected. In terms of bulk loading, the catalyst has a value of 2.2 mg cm^{-2}. In an aqueous electrolyte solution comprising 1.0 M potassium hydroxide, all the electrochemical measurements were performed. Generating curves for polarization at a rate of 10 mV s^{-1} was achieved by using the methodology of linear sweep voltammetry (LSV).

3. Results and discussions

The phase purity of the as-synthesized $Ti_{0.5}Sr_{0.5}O_3$ was validated through the utilization of the X-ray diffraction technique. An example of an XRD pattern for $Ti_{0.5}Sr_{0.5}O_3$ is shown in Fig. 1a, $Ti_{0.5}Sr_{0.5}O_3$, the peaks at 15.46°, 19.7°, 21.04°, 25.7°, 26.5°, 29.2°, 31.24°, 33.67°, 34.45°, 36.91°, 37.5°, 39.4°, 40.6°, 42.8°, 44.71°, 45.5°, 46.47°, 47.60°, 49.2°, 51.60°, 53.6°, 54.2°, 57.73°, 58.88°, 59.32°, 62.05°, 63.84°, 71.20°, 73.75°, 76.75°, 77.66°, 80.16°, 82.01°, 84.50°, and 85.77° are ascribed to the crystal planes of (111), (201), (211), (310), (301), (221), (002), (112), (202), (212), (330), (501), (402), (322), (520), (601), (003), (113), (213), (441), (223), (540), (630), (800), (333), (810), (513), (004), (314), (552), (334), (504), (434), (005), and (115) respectively. The XRD pattern of $Ti_{0.5}Sr_{0.5}O_3$, which revealed sharp diffraction peaks, indicating a high level of crystallinity.[15] All peaks can be appropriately shown, so that no impurity phase is present. The samples' diffraction peak shapes are prominent, demonstrating a high level of crystallinity. The findings demonstrate that the circular morphology was efficiently kept, whereas no defect molecules, including Ti–O or Sr–O, were identified.[16] All identified peaks can be attributed to the sphere structure. There is no indication of an impure phase. Sharp peaks can be attributed to a spherical arrangement with the $Fd\bar{3}m$ phase $P4_332$ phase. These predict that $Ti_{0.5}Sr_{0.5}O_3$ will have sharp, well-defined peaks indicate good crystallinity, which may influence electronic conductivity and stability. FT-IR spectral studies were utilized to evaluate the chemical composition of the as-prepared $Ti_{0.5}Sr_{0.5}O_3$ as well as the surface functional groups, as shown in Fig. 1b, demonstrating a band at 662.8 and 756.7 cm^{-1}, indicating Ti–O–Ti stretching vibrations.[17] Sharp bands at 819.8 and 872.5 cm^{-1} indicate Sr stretching and Sr–O vibrations, respectively. All of these peaks indicate the presence of Ti and Sr in the $Ti_{0.5}Sr_{0.5}O_3$ sample. Peaks at 1030.4 cm^{-1} correspond to TiO_2, 1093.8 and 3406.7 cm^{-1} for titanium, 1661.6 cm^{-1} for Ti–OH, 1293.3 cm^{-1} for CO stretching, and 1556.4 cm^{-1} for asymmetric stretching COO^- vibrations.[18] Raman spectroscopy was used to study the product structure based on lattice vibrations, showing characteristic peaks at 697.3, 776.1, 881.31, and 1070.6 cm^{-1}, which originate from $SrCO_3$; meanwhile, five peaks at 142.7, 200.2, 397.4, 513.3, and 636.7 cm^{-1} are attributed to TiO_2, indicating the existence of Ti and Sr in $Ti_{0.5}Sr_{0.5}O_3$ as shown in Fig. 1c.[19] The peaks at 142.7, 200.2, and 636.7 cm^{-1} correspond to the Raman prominent E_{1g}, E_{2g}, and A_{3g} symmetric stretching modes of titanium oxygen bonds.[20] The low-frequency bands at 397.4 and 513.3, attributed to B_{1g} + A_{1g}, correspond to symmetric modes.[21] The lateral peak at 636.7 cm^{-1} shows an atomic configuration that corresponds to the monoclinic $C2/m$ phase, in which the Ti atoms are linked to equatorial oxygen atoms. Raman analyses confirm that the monoclinic enhancement is a consequence of molecular chaotic behaviour caused by the uncertain configuration. In the course of solid-state reactions, changes in thermal effect and weight will occur.[22] These modifications will correspond to the formation and composition changes of the nano step-shaped facet that occur during the heating process. The thermal effect and weight changes will occur simultaneously. As a result, TGA and DTG were combined to perform a complete thermal study, as depicted in Fig. 1d. The initial weight loss happened when $Ti_{0.5}Sr_{0.5}O_3$ was heated from 50 to 400 °C due to the loss of hydroxyl molecules.[23] This could be attributed to the dehydration of absorbed fluids, as well as the disintegration of unreacted monomers and impurities in the sample.[24] Furthermore, the DTG curve revealed that the characteristic weight growth occurred at around 140 °C. The upward-projecting peak in the graph is assumed to represent the growth pattern of the nano step-shaped crystal facet. This is a hypothesis that has been advanced. When N_2 is subjected to the whole thermogravimetric test procedure, the weight rise at 160 °C is attributable to the entrance of an element into the lattice during crystal surface recombination. The curve returns to normal after 300 °C, indicating that N_2 is released from the lattice. The nanosphere forms during this process. According to the TGA–DTG findings, the temperature at which step-shaped crystal facet formation occurs is between 200 and 400 °C, which is also the temperature at which sphere surface reformation occurs.[25]

The porosity of $Ti_{0.5}Sr_{0.5}O_3$ has been examined employing the Brunauer–Emmett–Teller (BET) gas adsorption experiment. Fig. S6 reveals $Ti_{0.5}Sr_{0.5}O_3$ has type-IV isotherms with a discrete hysteresis loop. The size distribution curves illustrated mesoporosity, with several small and medium porous structures. The BET surface area of $Ti_{0.5}Sr_{0.5}O_3$ is 181 m^2 g^{-1}, with an average pore radius of 17.7 Å. The $Ti_{0.5}Sr_{0.5}O_3$ composite's high surface area and rich mesoporous structure allow for electrolyte access with active spots. The $Ti_{0.5}Sr_{0.5}O_3$ composite has a large surface area, pore volume (0.29 cc g^{-1}), and pore radius, permitting for a rapid electrolyte approach and effortless access to reactants with potential active sites.

As shown in Fig. 2a–d, the $Ti_{0.5}Sr_{0.5}O_3$ particle with a solid sphere structure is seen from the section of particles after calcinating the sample at 400 °C. Fig. S2 shows the resulting EDX profile. Peaks for titanium, strontium, carbon, and oxygen are

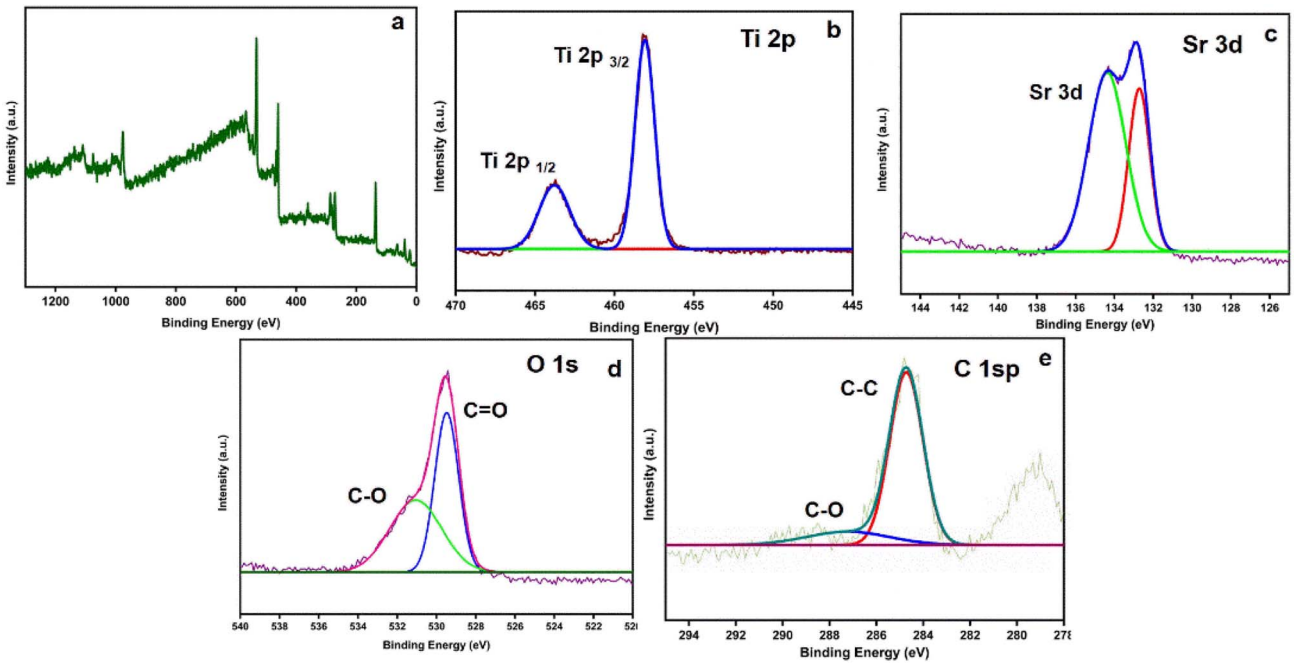

Fig. 3 XPS spectra; (a) XPS full survey spectra of $Ti_{0.5}Sr_{0.5}O_3$, (b) Ti 2p, (c) Sr 3d, (d) O 1s, and (e) C 1s.

present.[26] The calculated quantities of Ti, Sr, and O are 49.96, 38.87, and 11.7 wt%, based on the EDX profile's peak intensities. The determined number of metals in the sample is nearly identical to the TG analysis results, with only a slight change. Fig. 2i–l shows how elemental mappings supported the EDX study results. The elemental mappings clearly show the existence of all three elements (Ti, Sr, and O) with a uniform distribution, suggesting that the stoichiometry and stability of the bulk material are maintained. Notably, the intensities of Sr and Ti are higher, indicating that the processed sample is largely constituted of $Ti_{0.5}Sr_{0.5}O_3$. Fig. 2e and f demonstrates its high-resolution transmission electron microscopy (HRTEM) illustrations of $Ti_{0.5}Sr_{0.5}O_3$ nanosphere. Fig. 2g shows that the $Ti_{0.5}Sr_{0.5}O_3$ nano spherical sample exhibits two-dimensional lattice fringe patterns, implying that the nanocomposite is crystalline.[27] As expected, the estimated interplanar spacing values of about 0.08, 0.8, and 0.20 nm correlate to the (221), (002), and (212) planes of $Ti_{0.5}Sr_{0.5}O_3$, respectively, that is precisely indexed with $C/2m$ symmetry, indicating a spherically [002] $Ti_{0.5}Sr_{0.5}O_3$ phase. The Fast Fourier Transformation (FFT) of the HRTEM brings up the lattice fringe image, predicts the absence of defect and distortion, implying that $Ti_{0.5}Sr_{0.5}O_3$ has a high-quality crystal structure, the existence of all three elements (Ti, Sr, and O) with a uniform distribution, suggesting that the stoichiometry and stability of the bulk material are maintained. These faults were represented in the intensity of the XRD spectra, as well as in the homogeneous atomic distribution. Fig. 2h demonstrates the nanosized spherical $Ti_{0.5}Sr_{0.5}O_3$ nanoparticles through the SAED pattern. It displayed diffraction corresponding to (113), (221), (202), (002), and (213) planes of the $Ti_{0.5}Sr_{0.5}O_3$. Whereas the $Ti_{0.5}Sr_{0.5}O_3$ material has been ground into powder for this efficient evaluation, the image indicates an extensive number of spherical particles, thus being consistent with the SEM conclusions. The depicted pattern is distinguished by well-defined dots, which comprise clearly defined points and spirals, which validates the nanocomposites.[28] Additionally, the low defect concentration plays a significant role in frequent electron transport and also in titanium and strontium-ion insertion/extraction within the material.

The XPS spectra of $TiSrO_3$ in Fig. 3 show the predicted elemental states of the crystalline oxide. From Fig. 3b, the Ti 2p spectra demonstrated Ti^{4+} peaks at ~458 eV (Ti $2p_{3/2}$) and ~463 eV (Ti $2p_{1/2}$), revealing a spherical Ti–O lattice. A slight peak with lower binding energy indicates the presence of relatively small Ti^{3+} species, apparently due to oxygen vacancies. From Fig. 3c, the Sr 3d spectra exhibit doublet peaks at ~132.0 eV (Sr $3d_{5/2}$) and ~135 eV (Sr $3d_{3/2}$), showing lattice Sr^{2+}. A slightly higher binding energy contribution is attributed to surface hydroxylation or carbonate production. From Fig. 3d, the oxygen 1s spectrum can be separated into lattice oxygen (~529 eV) and surface hydroxyl groups (~531 eV), with a minor contribution from carbonate molecules (~532.5 eV).

4. Electrocatalytic activity evaluation

4.1 Oxygen evolution reaction (OER)

The OER activity occurring in $Ti_{0.5}Sr_{0.5}O_3$/NF had been evaluated by LSV in an electrolyte of 1.0 M KOH, as illustrated in Fig. 4a. Calcination at 400 °C enhanced the electrical conductivity in $Ti_{0.5}Sr_{0.5}O_3$/NF (1.65 V) when compared with RHE at 10 mA cm^{-2}, which was caused by enhanced particle size and significant phase shift due to mixed oxides.[29] The increased efficiency is attributable to the emergence of a spherical $Ti_{0.5}Sr_{0.5}O_3$/NF, which is suitable for strong electronic coupling along with rapid transfer of charge across the interface. The

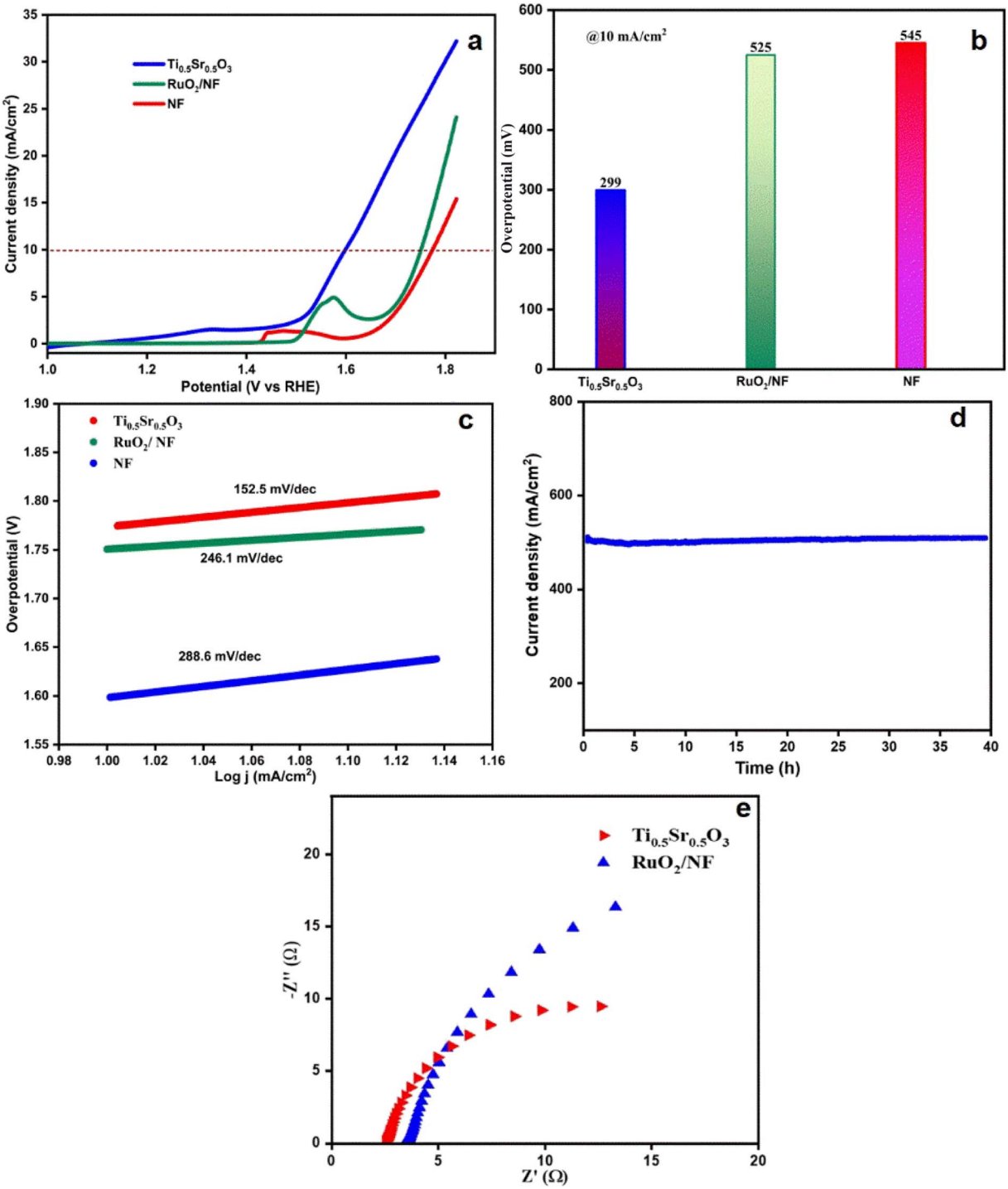

Fig. 4 (a) LSV curves; (b) comparison of the overpotential; (c) Tafel plots; (d) stability analysis; (e) Nyquist plot of $Ti_{0.5}Sr_{0.5}O_3$/NF.

redox-tolerant $Ti_{0.5}Sr_{0.5}O_3$/NF entity (Ti^{3+}/Ti^{4+}) plays an active role in the mechanism of reaction by consolidating oxygenation intermediary compounds (such as *OH, *OOH, *etc.*) and accelerating the O–O bond assembly stage.[30] These Ti and Sr sites, paired with the oxygen vacancies formed during annealing, augment the electrochemically active surface area, thereby enhancing intermediary retention. The synergistic interaction of Ti and Sr at the oxide interface improves the particle's electron configuration, which facilitates more rapid acceleration and better performance under oxidative conditions.[31] In general, the $Ti_{0.5}Sr_{0.5}O_3$/NF catalyst's exceptional OER effectiveness is attributable to the incorporation of several different Ti active sites, conductance mixed oxide phases, and interstitial charge propagation.

4.1.1 Stepwise mechanism of the OER in alkaline media. Step I: hydroxyl adsorption:

$$OH^- + * \rightarrow OH^* + e^-$$

Step II: formation of O*:

$$OH^* + OH^- \rightarrow O^* + H_2O + e^-$$

Step III: *OOH formation (rate-determining step):

$$O^* + OH^- \rightarrow OOH^* + e^-$$

Step IV: oxygen release:

$$OOH^* \rightarrow O_2 + * + H^+ + e^-$$

The synergistic interaction of $Ti_{0.5}Sr_{0.5}O_3$/NF surface, electrostatic, and structural properties resulted in its enhanced catalytic effectiveness in the hydrogen and oxygen evolution reaction. The electronic structure of the Ti sites, which are the principal active centers for hydrogen adsorption, is impacted by the surrounding oxygen framework and oxygen vacant spaces, which introduce Ti^{3+} states and raise the electron density at the active sites. Although they are not actively involved in hydrogen binding, the Sr atoms assist with stabilizing the lattice, modulating the covalency of the Ti–O bond, and influencing the perovskite's ultimate electronic conductivity, which promotes charge transfer throughout the reaction. In addition, hydroxyl groups and surface oxygen vacancies enhance water adsorption and dissociation, especially within alkaline conditions, minimizing the Volmer step's activation energy. These elements work together to generate near-optimal hydrogen adsorption free energies, lower reaction barriers, and improved electron mobility, all of which expedite the evolution of hydrogen. In contrast to stoicism of or vacancy-deficient surfaces alone, $TiSrO_3$ exhibits better electrocatalytic activity due to the synergy of structural stability, electronic variability, and surface reactivity.

To accomplish 10 mA cm^{-2}, $Ti_{0.5}Sr_{0.5}O_3$/NF required a minimum overpotential of 299 mV, in contrast with 525 mV for RuO_2 and 545 mV for pristine NF, as shown in Fig. 4b, which emphasizes the beneficial effect of thermal treatment on the performance of the catalyst.[32] Tafel slope computations in Fig. 4c proved a substantial reduction in slope for $Ti_{0.5}Sr_{0.5}O_3$ as 152.5 mV dec^{-1}, in contradiction to RuO_2 as 246.1 mV dec^{-1} and NF as 288.6 mV dec^{-1}. It therefore implies that $Ti_{0.5}Sr_{0.5}O_3$/NF demonstrates greater effectiveness of charge transfer and increased oxygen evolution kinetics, perhaps due to the resulting synergistic electronic interactions involving the Ti and Sr instances acquired during calcination over time. Due to the high conductivity of the electrolyte, the ohmic drop (*iR*) was negligible, and therefore compensation was not applied. The stability was tested after an initial 20-minute activation at 200 mA cm^{-2}. Chronoamperometry was employed to determine the longevity of the $Ti_{0.5}Sr_{0.5}O_3$/NF catalyst over 40 hours at a current density of 200 mA cm^{-2}, as illustrated in Fig. 4d. To further explore the diffusion of ion kinetics, electrochemical impedance spectroscopy (EIS) was employed. The precise longitudinal intercept in the region of high frequencies retrieves an indication of series resistance (R_s), which is the combined value of the resistance of the electrolyte, the inherent resistance of electrode material, and the resistance encountered during contact at the active material interface.[33] The Nyquist curve, as shown in Fig. 4e, demonstrates charge transfer resistance (R_{ct}), and the straight line depicts quasi-diffusion. $Ti_{0.5}Sr_{0.5}O_3$/NF, which exhibits lower charge transfer resistance (R_{ct}) and greater permeability at the electrode–electrolyte contact. Furthermore, the ECSA, as measured by double-layer capacitance (C_{dl}) about 2.05 mF cm^{-2} as shown in Fig. S3c, using CV profile in Fig. S3a, indicates a greater exploitable surface area and increased activity sites for the OER process. High-temperature annealing yields porous nanomaterials, and the improved roughness of the surface has been responsible for this enhancement.

4.2 Hydrogen evolution reaction (HER)

The hydrogen evolution reaction (HER) features of the generated catalysts were measured using linear sweep voltammetry, as shown in Fig. 5a. $Ti_{0.5}Sr_{0.5}O_3$/NF attained an overpotential of 101.6 mV at 10 mA cm^{-2}, concerning RuO_2 at 103.3 mV and NF as 115 mV, showing that, while $Ti_{0.5}Sr_{0.5}O_3$/NF has comparatively more significant values than RuO_2, it exhibits potential catalytic properties.[34] $Ti_{0.5}Sr_{0.5}O_3$/NF has better HER behavior, as illustrated by its shortest Tafel slope of 179 mV dec^{-1}, as shown in Fig. 5b, which indicates superior reaction kinetics along with quicker charge transfer stages, suggesting the excellent kinetics for the HER, which follows the Volmer–Heyrovsky mechanism. This augmentation could be related to the development of conductive $Ti_{0.5}Sr_{0.5}O_3$/NF hybrid structure during the calcined that increases the acquisition of hydrogen and promotes effective electron transport.

4.2.1 Stepwise mechanism of the HER in alkaline media. Step 1: water dissociation (rate-limiting in oxides):

$$\text{Ti site} + H_2O + e^- \rightarrow \text{Ti–H}^* + OH^-$$

Step 2: hydrogen evolution:
Heyrovsky pathway:

$$\text{Ti–H}^* + H_2O + e^- \rightarrow H_2 + OH^- + \text{Ti}$$

The Nyquist plots in Fig. 5c demonstrate that $Ti_{0.5}Sr_{0.5}O_3$ has the lowest charge transfer resistance of $Ti_{0.5}Sr_{0.5}O_3$/NF, which corresponds to its higher electrical conductivity and surface interaction dynamics. The electrochemical double-layer capacitance (C_{dl}) was measured using cyclic voltammetry (CV) in the non-faradaic potential range for determining the catalysts' electrochemical surface area (ECSA). CVs were computed at scan rates of 40, 80, 120, 120, 140, 160, 180, and 200 mV s^{-1}. The capacitive current density ($\Delta j = j_{anodic} - j_{cathodic}$ at the middle of the non-faradaic window) was plotted *versus* scan rate, with the

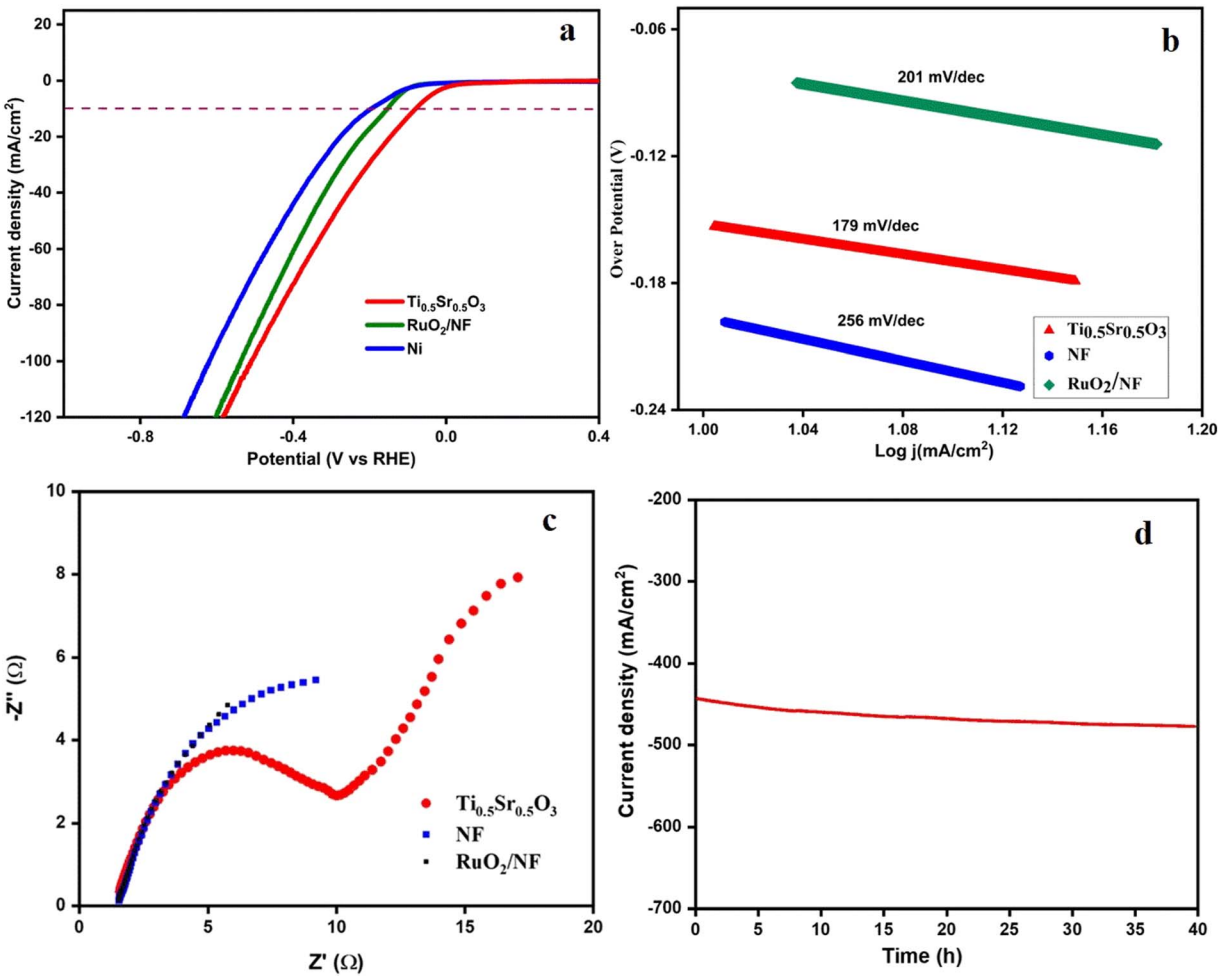

Fig. 5 (a) LSV curves; (b) Tafel plots; (c) Nyquist plot; (d) stability analysis of $Ti_{0.5}Sr_{0.5}O_3$/NF.

slope of the linear fit corresponding to C_{dl}. Furthermore, $Ti_{0.5}Sr_{0.5}O_3$/NF has the highest electrochemically active surface area of about 2.83 mF cm^{-2}, as evidenced by C_{dl} values as shown in Fig. S3c and obtained from CV curves as shown in Fig. S3b, indicating a greater number of exploitable sites that are active for HER.[35] The $Ti_{0.5}Sr_{0.5}O_3$/NF catalyst's long-term endurance was tested utilizing the chronoamperometry method at a constant voltage for 40 hours at a current density of 200 mA cm^{-2}, as shown in Fig. 5d.

Moreover, from Fig. S4b, the XRD diffraction pattern after stability testing shows that the characteristic reflections of $Ti_{0.5}Sr_{0.5}O_3$ are largely retained, indicating preservation of the bulk spherical structure. From Fig. S4a, the SEM images show that morphology remains generally intact, although slight surface roughening is observed. From Fig. S5a–e, XPS results show surface analysis reveals partial surface hydroxylation and a slight change in Ti oxidation state, suggesting surface reconstruction under water electrocatalytic conditions. These results indicate that while the bulk structure of $Ti_{0.5}Sr_{0.5}O_3$ remains stable, a thin amorphous (oxy)hydroxide layer likely forms at the surface during operation. This behavior is consistent with reported reconstruction phenomena in metal oxide OER catalysts and suggests that $Ti_{0.5}Sr_{0.5}O_3$ acts as a stable pre-catalyst under high current density.

5. Conclusion

The ultimate objective in this research is the development of stable, highly active, and cost-effective electrocatalysts for overall water splitting. As a result, a simple solid-state chemical process was used to create the $Ti_{0.5}Sr_{0.5}O_3$. Several characterization procedures were used to assess the nanocomposites' structural and morphological data. In alkaline environments, the composite demonstrated an effective electrocatalyst for the OER and HER. In a 1.0 M KOH solution, $Ti_{0.5}Sr_{0.5}O_3$/NF has good OER activity with overpotential and a Tafel slope of 299 mV and 152.5 mV dec^{-1}, respectively. It also exhibits strong HER activity, with overpotential, and has a Tafel slope of 101.6 mV and 179 mV dec^{-1}, respectively. These advantages are thought to be owing to the synergistic interaction of sphere phases, the electrostatic combustibility of Ti–Sr sites, improved surface accessibility, and an attractive spherical framework, all of which are confirmed by experimentation and theoretical findings. These findings show the potential of spherical $Ti_{0.5}Sr_{0.5}O_3$ based on transition metal oxides as electrocatalysts

that are both durable and efficient for use in environmentally friendly energy systems. Therefore, the prepared $Ti_{0.5}Sr_{0.5}O_3$ could be considered as an effective catalyst for water electrolyzer technology in the future.

Conflicts of interest

The authors declared that there are no conflicts of interest.

Data availability

Data will be made available on request.

Supplementary information (SI) is available. See DOI: https://doi.org/10.1039/d6ra00224b.

Acknowledgements

The authors acknowledge the financial support from the Department of Chemistry, SRM Institute of Science and Technology, Tamil Nadu-603203, India, and the Nanotechnology Research Centre (NRC), SRMIST, for providing the research facilities.

References

1 Y. Liu, P. Li, Z. Wang and L. Gao, Shape–Preserved CoFeNi–MOF/NF Exhibiting Superior Performance for Overall Water Splitting across Alkaline and Neutral Conditions, *Materials*, 2024, **17**, 2195.

2 T. Yu, *et al.*, Amorphous CoO_x-Decorated Crystalline RuO_2 Nanosheets as Bifunctional Catalysts for Boosting Overall Water Splitting at Large Current Density, *ACS Sustain. Chem. Eng.*, 2020, **8**, 17520–17526.

3 Y. Zhu, *et al.*, A Perovskite Nanorod as Bifunctional Electrocatalyst for Overall Water Splitting, *Adv. Energy Mater.*, 2017, **7**, 1602128.

4 J. Suntivich, K. J. May, H. A. Gasteiger, J. B. Goodenough and Y. A. Shao-Horn, Perovskite Oxide Optimized for Oxygen Evolution Catalysis from Molecular Orbital Principles, *Science*, 2011, **334**, 1383–1385.

5 Y. Lee, J. Suntivich, K. J. May, E. E. Perry and Y. Shao-Horn, Synthesis and Activities of Rutile IrO_2 and RuO_2 Nanoparticles for Oxygen Evolution in Acid and Alkaline Solutions, *J. Phys. Chem. Lett.*, 2012, **3**, 399–404.

6 M. P. Kumar, P. Murugesan, S. Vivek and S. Ravichandran, $NiWO_3$ Nanoparticles Grown on Graphitic Carbon Nitride (g-C_3N_4) Supported Toray Carbon as an Efficient Bifunctional Electrocatalyst for Oxygen and Hydrogen Evolution Reactions, *Part. Part. Syst. Charact.*, 2017, **34**, 1700043.

7 J. Zhang and D. Guo, Interfacial microenvironment modulation enhancing catalytic kinetics of CoNiP@NiFe LDH heterostructures for highly efficient oxygen evolution reaction, *RSC Adv.*, 2023, **13**, 28583–28589.

8 S. Ullah, *et al.*, Molybdenum tungsten hydrogen oxide doped with phosphorus for enhanced oxygen/hydrogen evolution reactions, *RSC Adv.*, 2024, **14**, 27928–27934.

9 P. K. Sahoo, S. R. Bisoi, Y.-J. Huang, D.-S. Tsai and C.-P. Lee, 2D-Layered Non-Precious Electrocatalysts for Hydrogen Evolution Reaction: Fundamentals to Applications, *Catalysts*, 2021, **11**, 689.

10 L. Xia, *et al.*, Structural engineering of hierarchically heterostructured Mo_2C/Co conformally embedded in carbon for efficient water splitting, *Int. J. Hydrogen Energy*, 2020, **45**, 22629–22637.

11 B. Song, *et al.*, Tuning Mixed Nickel Iron Phosphosulfide Nanosheet Electrocatalysts for Enhanced Hydrogen and Oxygen Evolution, *ACS Catal.*, 2017, **7**, 8549–8557.

12 K. Rajagopal, P. Suresh, A. Rajaram and A. Natarajan, A novel Co-precipitation assisted $Li_{1.05}Ni_{0.5}Mn_{1.40}Ce_{0.10}O_4$ spinel as an eloquent electrocatalyst for methanol oxidation, *Chem. Phys. Lett.*, 2023, **823**, 140518.

13 H. Yang, M. Zhu, X. Guo, C. Yan and S. Lin, Anchoring $MnCo_2O_4$ Nanorods from Bimetal-Organic Framework on rGO for High-Performance Oxygen Evolution and Reduction Reaction, *ACS Omega*, 2019, **4**, 22325–22331.

14 D. Wang, Q. Li, C. Han, Z. Xing and X. Yang, When NiO@Ni Meets WS_2 Nanosheet Array: A Highly Efficient and Ultrastable Electrocatalyst for Overall Water Splitting, *ACS Cent. Sci.*, 2018, **4**, 112–119.

15 Y. Wu, B. Dong, J. Zhang, H. Song and C. Yan, The synthesis of ZnO/$SrTiO_3$ composite for high-efficiency photocatalytic hydrogen and electricity conversion, *Int. J. Hydrogen Energy*, 2018, **43**, 12627–12636.

16 C. Chen, *et al.*, $K_{0.5}Na_{0.5}NbO_3$-$SrTiO_3$/PVDF Polymer Composite Film with Low Remnant Polarization and High Discharge Energy Storage Density, *Polymers*, 2019, **11**, 310.

17 N. Rajkoomar, A. Murugesan, S. Prabu and R. M. Gengan, Synthesis of methyl piperazinyl-quinolinyl α-aminophosphonates derivatives under microwave irradiation with Pd–$SrTiO_3$ catalyst and their antibacterial and antioxidant activities, *Phosphorus, Sulfur Silicon Relat. Elem.*, 2020, **195**, 1031–1038.

18 P.-S. Konstas, I. Konstantinou, D. Petrakis and T. Albanis, Development of $SrTiO_3$ Photocatalysts with Visible Light Response Using Amino Acids as Dopant Sources for the Degradation of Organic Pollutants in Aqueous Systems, *Catalysts*, 2018, **8**, 528.

19 M. Akilarasan, *et al.*, An eco-friendly low-temperature synthetic approach towards micro-pebble-structured GO@$SrTiO_3$ nanocomposites for the detection of 2,4,6-trichlorophenol in environmental samples, *Microchim. Acta*, 2021, **188**, 72.

20 H. Li, *et al.*, Lattice distortion embedded core–shell nanoparticle through epitaxial growth barium titanate shell on the strontium titanate core with enhanced dielectric response, *Adv. Compos. Hybrid Mater.*, 2022, **5**, 2631–2641.

21 A. Vijay, K. Bairagi and S. Vaidya, Relating the structure, properties, and activities of nanostructured $SrTiO_3$ and SrO–$(SrTiO_3)_n$ (n = 1 and 2) for photocatalytic hydrogen evolution, *Mater. Adv.*, 2022, **3**, 5055–5063.

22 E. Li, Y. Shi, C. Sun, Y. Zhao and S. Zhang, Effect of $SrTiO_3$ on the properties of CBS glasses/Al_2O_3 ceramics, *J. Mater. Sci.: Mater. Electron.*, 2016, **27**, 6592–6597.

23 M. A. K. Y. Shah, *et al.*, Semiconductor Nb-Doped $SrTiO_{3-\delta}$ Perovskite Electrolyte for a Ceramic Fuel Cell, *ACS Appl. Energy Mater.*, 2021, **4**, 365–375.

24 M. H. El-Sadek, M. M. Farahat, H. H. Ali and Z. I. Zaki, Synthesis of $SrTiO_3$ from celestite and rutile by mechanical activation assisted Solid-State reaction, *Adv. Powder Technol.*, 2022, **33**, 103548.

25 G. Chen, *et al.*, Electrochemical mechanisms of an advanced low-temperature fuel cell with a $SrTiO_3$ electrolyte, *J. Mater. Chem. A*, 2019, **7**, 9638–9645.

26 K. Ujiie, T. Kojima, K. Ota, S. Hosoya and N. Uekawa, Low-temperature synthesis of strontium titanate particles with high specific surface area, *J. Ceram. Soc. Jpn.*, 2021, **129**, 21085.

27 A. Nakamura, *et al.*, Room-Temperature Plastic Deformation of Strontium Titanate Crystals Grown from Different Chemical Compositions, *Crystals*, 2017, **7**, 351.

28 S. Huh, *et al.*, Solvothermal Synthesis and Interfacial Magnetic Interaction of β-FeSe/$SrTiO_{3-x}$ Nanocomposites, *ChemistrySelect*, 2020, **5**, 9517–9522.

29 P. Kaleeswarran, *et al.*, $FeTiO_3$ Perovskite Nanoparticles for Efficient Electrochemical Water Splitting, *Catalysts*, 2021, **11**, 1028.

30 K. Rajagopal, M. Kathiresan, A. Rajaram, A. Natarajan and K. Natesan, Development of robust noble-metal free lanthanum, neodymium doped $Li_{1.05}Ni_{0.5}Mn_{1.5}O_4$ as a bifunctional electrocatalyst for electrochemical water splitting, *RSC Adv.*, 2023, **13**, 23829–23840.

31 X. Lei, *et al.*, Self-generated $FeSe_2$ and $CoSe_2$ nanoparticles confined in N, S-doped porous carbon as an efficient and stable electrocatalyst for oxygen evolution reaction, *Electrochim. Acta*, 2023, **445**, 142049.

32 Y. Liu, *et al.*, Porous Mn-doped cobalt phosphide nanosheets as highly active electrocatalysts for oxygen evolution reaction, *Chem. Eng. J.*, 2021, **425**, 131642.

33 X. Zhao, *et al.*, Electrical and structural engineering of cobalt selenide nanosheets by Mn modulation for efficient oxygen evolution, *Appl. Catal., B*, 2018, **236**, 569–575.

34 N. Liu, Z. Duan, Q. Zhang and J. Guan, Insights into active species of ultrafine iridium oxide nanoparticle electrocatalysts in hydrogen/oxygen evolution reactions, *Chem. Eng. J.*, 2021, **419**, 129567.

35 Q. Zhang and J. Guan, Atomically dispersed catalysts for hydrogen/oxygen evolution reactions and overall water splitting, *J. Power Sources*, 2020, **471**, 228446.